

Impact of 3-D urban landscape patterns on the outdoor thermal environment: a modelling study with SOLWEIG

Article

Accepted Version

Kong, F., Chen, J., Middel, A., Yin, H., Li, M., Sun, T. ORCID: <https://orcid.org/0000-0002-2486-6146>, Zhang, N., Huang, J., Liu, H., Zhou, K. and Ma, J. (2022) Impact of 3-D urban landscape patterns on the outdoor thermal environment: a modelling study with SOLWEIG. Computers, environment and urban systems, 94. 101773. ISSN 0198-9715 doi: 10.1016/j.compenvurbsys.2022.101773 Available at <https://centaur.reading.ac.uk/103830/>

It is advisable to refer to the publisher's version if you intend to cite from the work. See [Guidance on citing](#).

To link to this article DOI: <http://dx.doi.org/10.1016/j.compenvurbsys.2022.101773>

Publisher: Elsevier

All outputs in CentAUR are protected by Intellectual Property Rights law, including copyright law. Copyright and IPR is retained by the creators or other copyright holders. Terms and conditions for use of this material are defined in the [End User Agreement](#).

www.reading.ac.uk/centaur

CentAUR

Central Archive at the University of Reading

Reading's research outputs online

**Impact of 3-D urban landscape patterns on the outdoor thermal environment: A
modelling study with SOLWEIG**

Fanhua KONG^{*,1}, Jianyu CHEN², Ariane Middel³, Haiwei YIN⁴, Manchun LI¹, Ting
SUN⁵, Ning Zhang⁶, Jing HUANG¹, Hongqing LIU¹, Kejing ZHOU¹, Jinsong MA¹

¹ School of Geography and Ocean Science, Nanjing University, Xianlin Ave.163, 210023,
Nanjing, China

² SPIC Energy Technology& Engineering Co., LTD, Tianlin Ave. 888#7, 200233, Shanghai,
China

³ School of Arts, Media and Engineering, Arizona State University, 950 S. Forest Mall,
Stauffer B258, 85281 Tempe, Arizona, USA

⁴ School of Architecture and Urban Planning, Nanjing University, No. 22, Hankou Road,
210093, Nanjing, China

⁵ Department of Meteorology, University of Reading, Reading RG6 6ET, UK

⁶ School of Atmospheric Sciences, Nanjing University, Xianlin Ave.163, 210023, Nanjing,
China

Impact of 3-D urban landscape patterns on the outdoor thermal environment: A modelling study with SOLWEIG

Abstract: With global warming and rapid urban growth, cities get warmer, which poses additional stress on human thermal comfort and health. Complex three-dimensional (3D) urban forms change radiation fluxes and shade patterns in cities, but most studies that link urban form to thermal exposure have traditionally investigated the horizontal, two-dimensional composition and configuration of urban landscapes. Supported by high-precision airborne LiDAR data and IKONOS satellite data, this study calculates 3D urban landscape metrics for central Nanjing, China, including vegetation above ground biomass (AGB), building volume (V_B), standard deviation of building and vegetation heights (HSD_B , HSD_V), the building normalized compactness ratio (nCR), sky view factor (SVF), surface roughness (SR), and shadow patterns (SP). Diurnal hourly mean radiant temperature (T_{mrt}) is simulated using the UMEP (Urban Multi-scale Environmental Predictor) tool forced with fixed-point observation data for a typical hot summer day. Correlation and multiple regression analyses are conducted to investigate the relationship between the 3D form metrics and T_{mrt} and to identify key factors that influence the thermal environments. T_{mrt} varies spatially and diurnally and is strongly related to SP during the day, revealing the importance of solar access for modulating the thermal environment. AGB is negatively, but SVF , SP , and building nCR are positively correlated with daytime T_{mrt} . At night, T_{mrt} is more homogeneous across space and mainly impacted by the urban fabric's ability to lose heat. Open areas cool faster than areas with low SVF and complex urban forms with high building nCR . Findings from this study have great scientific and practical significance for optimizing urban landscape patterns from a human-centered heat exposure perspective and will guide planning and

1
2
3
4
5
6
7
8
9
10
11
12
13
14
15
16
17
18
19
20
21
22
23
24
25
26
27
28
29
30
31
32
33
34
35
36
37
38
39
40
41
42
43
44
45
46
47
48
49
50
51
52
53
54
55
56
57
58
59
60
61
62
63
64
65

24 design strategies to promote thermally comfortable urban environments.

25 **Keywords:** Three-dimensional urban landscape metrics, urban thermal environment, mean

26 radiant temperature, LiDAR, UMEP

27

1. Introduction

Livability, health, and sustainable development of cities are key issues of the Anthropocene in the face of climate change. Urbanization converts natural spaces into man-made impervious spaces and meanwhile, building density and height increase continuously as urban areas develop and expand. Changes in the composition and configuration of urban landscapes directly affect the urban thermal environment, resulting in significant intensification of the urban heat island (UHI) (Oke et al., 1981; Santamouris et al., 2014; Solcerova et al., 2017). Additionally, with climate change, the intensity, duration, and frequency of heat waves in cities increase, leading to a decrease in outdoor thermal comfort and added heat stress on urban dwellers (Patz et al., 2005; Perkins et al., 2012; Li et al., 2020).

The main incoming energy source in the urban canopy layer is the solar radiation received at the surface. The composition and configuration of three-dimensional (3D) urban landscape patterns affect how much direct radiation enters an urban canyon, how it is reflected, and how much heat is stored and emitted (Bonan, 2015; Zhu et al., 2020). In cities, buildings are major urban landscape elements. Building volumes and materials and their arrangement affect the thermal storage capacity and energy transmission processes of the city (Salata et al., 2015). Differences in building height and density can cause multiple reflections of sunlight irradiated on the building surface, causing reabsorption (Yang & Li, 2015; Ronchi et al., 2020). Street morphology, especially the ratio of building height to street width (H/W ratio), typically affects the radiative environment (Park et al., 2021). At night, heat is trapped in narrow streets, thereby increasing air temperature, but more surface shading during the day leads to cooling (Aboelata, 2020). Studies have also shown that the normalized compactness ratio (nCR) (Bonczak & Kontokosta, 2019), sky view factor (SVF) (Middel et

al., 2018), urban shade (Hwang et al., 2011; Peters, 2016), and surface roughness (Maragkogiannis et al., 2014; Zhang et al., 2018) affect the thermal environment.

Urban green spaces play a critical role in mitigating the UHI and regulating the thermal environment. Previous studies have demonstrated that two-dimensional (2D) green space metrics, such as area and shape of vegetation, affect the urban thermal environment; generally, the larger the area is, the more pronounced the cooling effect (Kong et al., 2014; Motazedian et al., 2020). Additionally, the three-dimensional (3D) characteristics of vegetation also affect the thermal environment, creating a specific local microclimate (Chun & Guldman, 2018; Zellweger et al., 2019; Zhang et al., 2019). Research has shown that the aboveground biomass (*AGB*) of vegetation affects cooling (Chun & Guldman, 2014). Leaves absorb part of the incident solar radiation and convert a small part of the radiation energy into chemical energy through photosynthesis, thereby reducing the ambient temperature (Rahman et al., 2020). In addition, most of the radiant energy absorbed by vegetation is used for transpiration, which cools the environment and increases humidity (Hsieh et al., 2018). Moreover, the vegetation canopy shades ground surfaces and building façades, which reduces the absorption of solar radiation in the urban fabric (Wong & Yu, 2005; Bowler et al., 2010; Norton et al., 2015).

Outdoor human activities and health are mainly affected by urban near-surface temperature and radiant flux densities the human body is exposed to. The mean radiation temperature (T_{mrt}) refers to the shortwave and longwave radiation that irradiates a person from all directions, including direct and reflected radiation. It is one of the most important meteorological parameters regulating the human energy balance and human thermal comfort (Thorsson et al., 2007; Middel et al., 2021). T_{mrt} considers the radiative influence of ground

surfaces, building façades, and vegetation. It characterizes how a person perceives thermal conditions more comprehensively than surface temperature or air temperature, especially under hot conditions ([Middel & Krayenhoff, 2019](#)).

Most studies that investigate the impact of urban landscapes on temperatures are limited to 2D ([Amiri et al., 2009](#); [Li et al., 2016](#)). However, 2D urban landscape patterns fail to represent the spatial heterogeneity of complex 3D structures, which may impact the thermal capacity, thermal conductivity, and thermal radiation in complex built environments. Additionally, it is difficult to scientifically guide real-world urban planning and development based on research conclusions drawn from a 2D landscape perspective ([Chen et al., 2014](#)). Therefore, 3D landscape patterns must be scientifically quantified to comprehensively assess the impact of urban form on outdoor thermal environments.

In recent years, the rapid development of multisource remote sensing data, especially LiDAR remote sensing technology, has provided important support for obtaining and quantifying 3D urban landscape elements at fine scales. At the same time, advances in numerical simulation models for multiscale thermal environments facilitate comprehensive analyses of 3D urban morphological impacts on the thermal environment. Past LiDAR-based urban form studies investigated vertical characteristics of urban landscapes by creating metrics such as the average, minimum, and maximum height of buildings ([Zimble et al., 2003](#); [Petras et al., 2017](#)). At present, land cover composition and configuration studies that consider height metrics still cannot fully reveal the impact of 3D urban form on the ability of urban surfaces to receive and emit radiation, because they lack information on radiant fluxes and shade. In addition, most studies focus on remotely sensed land surface temperature, because fine-scale radiant flux densities are not readily available for cities. There is a lack of

research that investigates the influence of 3D urban landscape patterns on the thermal environment from the perspective of outdoor thermal comfort.

This research gap has great scientific and practical significance for optimizing urban landscape patterns from a human-centered heat exposure perspective. The present study constructs 3D urban landscape metrics retrieved from high-resolution airborne LiDAR point clouds coupled with numerical simulations of the radiant environment and shade to assess the impact of 3D urban form on the summer thermal environment for central Nanjing, China. Based on micrometeorological data from fixed-point observations, radiative fluxes and shade patterns are simulated with the urban multiscale environmental predictor (UMEP) model to explore the thermal spatial heterogeneity and investigate its relationship with 3D urban form. This study will guide the optimization of urban planning and development patterns to alleviate urban heat.

2. Data and methods

2.1. Study area

The study was conducted in Nanjing, capital of the Jiangsu Province in China in the west of the Yangtze Delta (Fig. 1). Nanjing has a subtropical monsoon climate with four seasons and a hot and humid summer. The mean daily maximum temperature between June and August is 31 °C (Nanjing Meteorological Bureau). The number of hot days per year and the frequency of heat waves have been increasing, with 112 summer heat wave events (defined as three consecutive days with temperature ≥ 35 °C) between 1951 and 2009 (Xu et al., 2011; Kong et al., 2016). Nanjing has an urban built-up area of 971.62 km² and a population of 6,959,900. Spatial urbanization patterns are constantly changing due to continuous horizontal and vertical urban growth. Nanjing has experienced outward

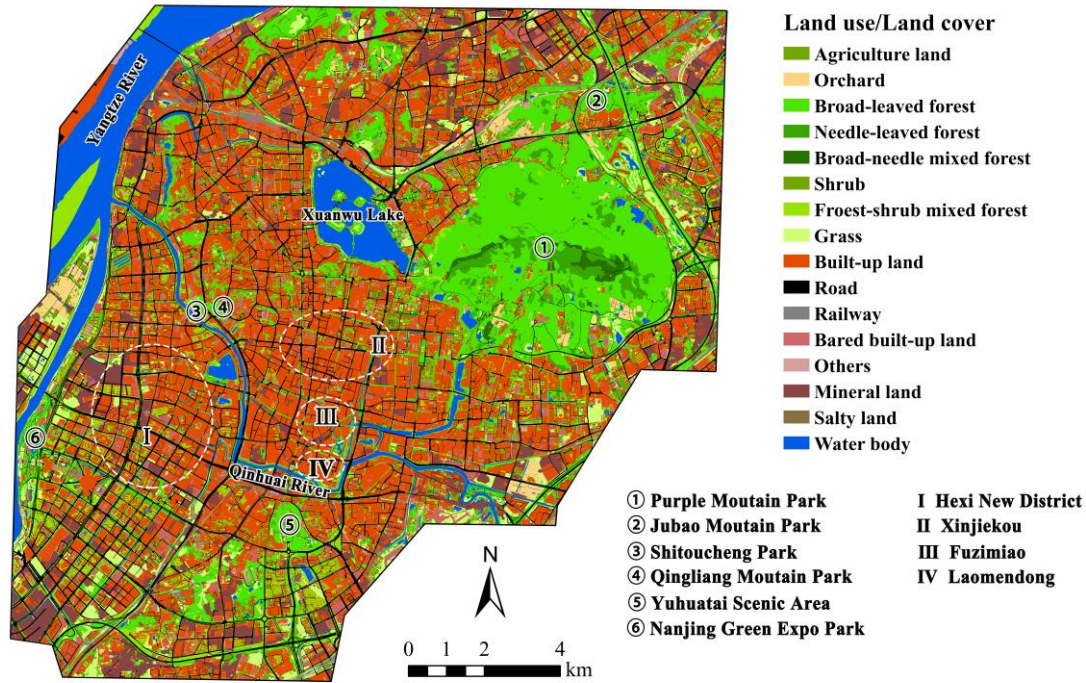


Fig.1 Land use /land cover, main parks and locations of the study area in Nanjing

2.2 UMEP tool and data processing

The UMEP tool is a plug-in for QGIS that can be used for various urban applications, such as outdoor thermal comfort, energy consumption, and climate change adaptation on an urban scale (Lindberg et al., 2018; Gabey et al., 2019). UMEP allows for interacting with QGIS-based spatial information and using different data sources (Abbasabadi & Ashayeri, 2019; Fernández et al., 2021). This study uses the UMEP Urban Geometry module and the Outdoor Thermal Comfort module to calculate SVF, SP , and T_{mrt} for Nanjing. Based on the 2-m resolution DEM, high resolution T_{mrt} maps are generated using SOLWEIG (SOLar and LongWave Environmental Irradiance Geometry model). SOLWEIG is part of UMEP and

estimates shortwave and longwave radiation fluxes based on the urban geometry (eg. SVF) (Lindberg et al., 2008; Ratti et al., 2006), vegetation, geographic information (latitude, longitude, and elevation), and meteorological forcing data (direct and diffuse radiation, global radiation, air temperature, and relative humidity).

To understand the spatiotemporal variation of T_{mrt} in central Nanjing, this study selected August 7, 2013 as simulation date, because weather conditions were typical of a clear, hot summer day in Nanjing. Statistical analyses were conducted for six hours of the day: 10:00h, 12:00h, 14:00h, 16:00h, 20:00h, and 22:00h. To analyze the impact of 3D urban form on T_{mrt} , the 2-m resolution UMEP output is aggregated to a 120-m grid. SPSS 26.0 was used to conduct bivariate correlation analyses and stepwise multivariate linear regressions for the 3D urban landscape metrics and T_{mrt} to identify the key factors affecting the thermal environment.

2.3 Data sources and preprocessing

This study uses four data sources to determine 3D urban landscape metrics and T_{mrt} for central Nanjing: fixed-point weather station data, airborne LiDAR data, a national vector dataset with detailed building footprints and land use/cover information (the second national land resource survey was conducted between 2007 and 2009), and IKONOS remote sensing images. The airborne LiDAR data were acquired by the City of Nanjing in April 2009 as part of a municipal effort to build a geospatial database. The LiDAR data were pre-processed and analyzed using the LiDAR360 software (GreenValley International Ltd 2019, Berkeley, California). A high-resolution urban normalized digital surface model (nDSM) and digital elevation model (DEM) were derived from the point cloud as basis for the 3D urban landscape metrics. The national vector dataset was used as mask to extract the 3D urban landscape metrics from LIDAR at 2-m resolution. High spatial resolution IKONOS remote

sensing images from 2009 served as virtual reference data to check the urban landscape classification.

The UMEP model requires air temperature, relative humidity, and direct and diffuse solar radiation to simulate T_{mrt} . For meteorological forcing, hourly observations were obtained from a weather station in Downtown Nanjing (Table 1) for 24 hours on August 7, 2013—a typical hot summer day with clear skies.

Table 1 Hourly meteorological observations to force the UMEP model, corresponding sensors, and installation height.

Parameters	Instruments	Installation Height (m)
Net Radiation	pyranometer (4-Component net radiometer, CNR4, Campbell Scientific Inc., USA)	1.5
Long-wave Radiation	pyranometer (4-Component net radiometer, CNR4, Campbell Scientific Inc., USA)	1.5
Latent Heat	EC150, Campbell Scientific Inc., USA	1.5
Relative Humidity	temperature and RH probe (HMP155A, Scientific Inc., USA)	4,9,18,36,72
Wind Speed	2-D sonic Anemometers (010C and 020C, Campbell Scientific Inc., USA)	4,9,18,36,72
Air Temperature	temperature and RH probe (HMP155A, Scientific Inc., USA)	4,9,18,36,72
Precipitation	rain gage (TE525WS-L, Campbell, USA)	1

2.4 Three-dimensional urban landscape metrics

The IKONOS classified land cover data was intersected with the high-resolution nDSM to generate a separate building nDSM (nDSM-B) and vegetation nDSM (nDSM-V) of central Nanjing. The two surface models form the basis to calculate four 3D urban landscape metrics on a 2-m × 2-m grid. Additional metrics are calculated using UMEP at a 2-m resolution. The 3D urban landscape metrics are then used in statistical analyses to assess the impact of 3D

urban form on the thermal environment.

2.4.1. Sky view factor (SVF)

The SVF, which is defined as the amount of visible sky in the upper hemisphere (Johnson and Watson, 1984; Middel et al., 2018), is an important metric to quantify urban morphology, because it modulates how much solar radiation enters and leaves an urban street canyon. The SVF has been shown to impact air temperature (Oke, 1988; Chen et al., 2012), ventilation (Grimmond and Oke, 1999), solar radiation, and T_{mrt} (Lindberg & Grimmond, 2011; Middel et al., 2018). Kidd and Chapman (2012) were the first to propose generating single-point and continuous SVFs based on high-resolution LiDAR data. In traditional SVF calculations, vegetation information is either omitted, or simple models (e.g., rectangular columns and ellipsoids) are used to replace trees, thereby posing a challenge to quantify the impact of vegetation in detail. An et al. (2014) analyzed the impact of vegetation canopy on SVF based on high-precision 3D point cloud (3DPC) data. The direct use of 3DPC to obtain SVF can be computationally intensive, but derived products (DEM and DSM) can be used instead (Zakšek et al., 2011). Continuous SVFs can be calculated using the preprocessing module of the UMEP tool, which implements a shadow casting algorithm based on raster data (Ratti and Richens, 1999). In this study, SVF data at 2-m resolution are obtained using the high-resolution DSM of Nanjing.

2.4.2. Standard deviations for building and vegetation height

The vertical variability of an urban area can be quantified using the standard deviation of the average building height (HSD_B) and vegetation height (HSD_V). Building height directly influences the solar radiation received by an urban canyon, as it impacts SVF. Areas with taller buildings and lower SVF have been shown to increase the nocturnal UHI (Oke, 1981;

Unger, 2009) but improve daytime thermal conditions due to shading (Ali-Toudert and Mayer, 2007; Middel et al., 2014; Mirzaee et al., 2018). Taller and larger trees increase canopy coverage and shading of ground surfaces, thereby reducing the solar radiation absorbed by the ground during the day and reducing surface temperature (Bowler et al., 2010). Heterogeneous vertical urban forms increase roughness in the urban canopy layer, resulting in more complex reflection and absorption of solar radiation. Considering the scale difference of individual buildings and vegetation and the relatively large plane area of building roofs, HSD_B is calculated using a grid of 120-m with a resampling resolution of 2-m, and $HSD_{B(V)}$ is calculated as follows:

$$HSD_{B(V)} = \sqrt{\sum_{i=1}^n \frac{(H_{B(V)i} - \bar{H}_{B(V)})^2}{n}} \quad (1)$$

where $HSD_{B(V)}$ is the standard deviation of building and vegetation height, respectively; $H_{B(V)i}$ is the height of the sample within the unit area; $\bar{H}_{B(V)}$ is the average height of the unit area; and n is the number of samples within the unit area.

2.4.3. Building volume (V_B) and aboveground biomass (AGB)

The building volume V_B is correlated to the height and envelope of a structure. Tall buildings are less likely to be shaded by other surrounding structures, thus they absorb more solar radiation and have increased roof surface temperatures (Sharmin et al., 2012; Perini & Magliocco, 2014; Shareef & Abu-Hijleh, 2020). Similarly, the size of the building envelope affects the heat capacity of a building and determines the amount of heat it can store during the day, affecting the UHI at night (Givoni, 1998). In turn, the AGB of vegetation impacts evapotranspiration and shading (Michiles & Gielow, 2008). V_B and AGB within the unit area of a 2-m grid are calculated using the following equations:

$$V_{Bi} = H_{Bi} \times S$$

$$AGB_i = H_{Vi} \times S \quad (2)$$

where V_{Bi} and AGB_i are the V_B and AGB within the i th unit area, $H_{B(V)i}$ is the raster elevation of buildings (or vegetation) within the i th unit area, and S is the base area of the unit area (2-m \times 2-m).

2.4.4. Building compactness ratio (CR)

The building compactness ratio (CR) is the ratio of building surface area to V_B within a unit area and is a metric in building morphology that describes the complexity of building structures. Subsequently, the normalized CR (nCR) is defined as the envelope surface area per unit building volume. As a metric characterizing the complexity of building surface structure, nCR is mostly applied in large-scale urban studies and rarely used as a landscape metric parameter in urban thermal studies.

Thus far, the impact of compact development on the urban thermal environment has been mostly studied in the context of land surface temperature (Li et al., 2016) but not with respect to T_{mrt} . The normalized CR (nCR) is calculated based on CR using the following equation (Bonczak & Kontokosta, 2019):

$$CR_i = S_{ei} \div V_{Bi} \quad (3)$$

$$nCR_i = \frac{CR_i}{((\sqrt[3]{V_{Bi}})^2 \times 5) \div V_{Bi}} = \frac{S_{ei}}{(\sqrt[3]{V_{Bi}})^2 \times 5} \quad (4)$$

Where CR_i is the building compactness ratio and nCR_i is normalized within the i th 120-m grid respectively; S_{ei} is the building envelope surface area and V_{Bi} is V_B within the i th 120-m grid; building envelope surface area of each 2-m \times 2-m grid S_{e2} was computed using the following equation:

$$S_{ez} = S / \cos([Slope] \times \pi / 180) \quad (5)$$

Where S is the area of the 2-m grid, and *slope* can be computed based on nDSM-B using the ArcGIS 3D Analyst extension (Vers. 10.5) (ESRI, Redlands, CA, USA) and the S_{ei} then be statistically computed using the “zonal statistics” (Zhang et al., 2011; Jenness, 2004).

2.4.5. Daily Shadow Patterns (SP)

The daily shadow pattern (*SP*) is a shade metric that changes with the position of the sun in the sky (azimuth and zenith angles). The shadow patterns on the ground originate from DSM of buildings, topography, trees and bushes using the Shadow generator plugin, and the position of the sun is calculated using PySolar, a python library for various sun related applications (Lindberg & Grimmond, 2011; Lindberg et al., 2018). The *SP* characterizes the direct solar radiation received by an area at a specific time of day, day of the year, and geographic location depending on the surrounding urban form. The amount of direct incoming solar radiation is a main driver of T_{mrt} during the day (Middel & Krayenhoff, 2019; Peeters et al., 2020). *SP* can have three transmittance values: 0 (completely shaded, e.g., by a building), 1 (completely sun-exposed), and 0.03 (shaded by vegetation). In this study, a *SP* map is produced in the UMEP SOLWEIG Analyzer using the 2-m resolution DSM.

2.4.6. Surface roughness (SR)

Buildings and vegetation create a rough surface in the urban canopy layer (Oke, 1989). Heterogeneous vertical urban forms increase surface roughness (*SR*), which impacts turbulence and ventilation (Barlow, 2014). The *SR* is an index to measure the surface (including building and vegetation) texture or fluctuation, which has been used in air quality and meteorological models to account for enhanced mixing and the drag effects of the

underlying surface and measured in different way (Duan & Takemi, 2021; Nield et al., 2013; Grimmond & Oke, 1999). The higher SR , the greater the resistance to wind, which impedes the flow of energy. SR_i is calculated as the ratio of the surface area per unit building or vegetation envelope surface area S_{ei} to the corresponding vertical projected area (S_{pi}) (unit area size 120-m \times 120-m):

$$SR_i = \frac{S_{ei}}{S_{pi}} \quad (6)$$

Where SR_i is the surface roughness, S_{ei} is the envelope surface area which can be computed according to equation (5), and S_{pi} is vertical projected planimetric area within the i th 120-m grid.

3. Results

3.1 Urban landscape pattern characteristics

3.1.1 Three-dimensional characteristics of vegetation and buildings

The AGB of vegetation in central Nanjing varies significantly (Fig 2(a)). Areas with high AGB are mainly clustered in parks (Fig 2(a), ①-⑤), especially at Purple Mountain (Fig 2(a), ①), a remnant hilly landscape with high vegetation cover and dense forest. In contrast, the southwestern Hexi New District—a newly urbanized area with little vegetation—has much lower AGB (Fig 2(a), I). Areas with high AGB also exhibit greater vertical variability. HSD_V is largest at the park area, which are natural forest areas in the city with diverse vegetation, mixed forest, shrubs, and grass (Fig 2(b), ①-⑤). HSD_V is also large on both sides of the streets in the Xinjiekou-Laomendong area (Fig 2(b), II- IV), which is the Old Town of Nanjing. Street trees are dominated by *Platanus orientalis* Linn trees and well-growing

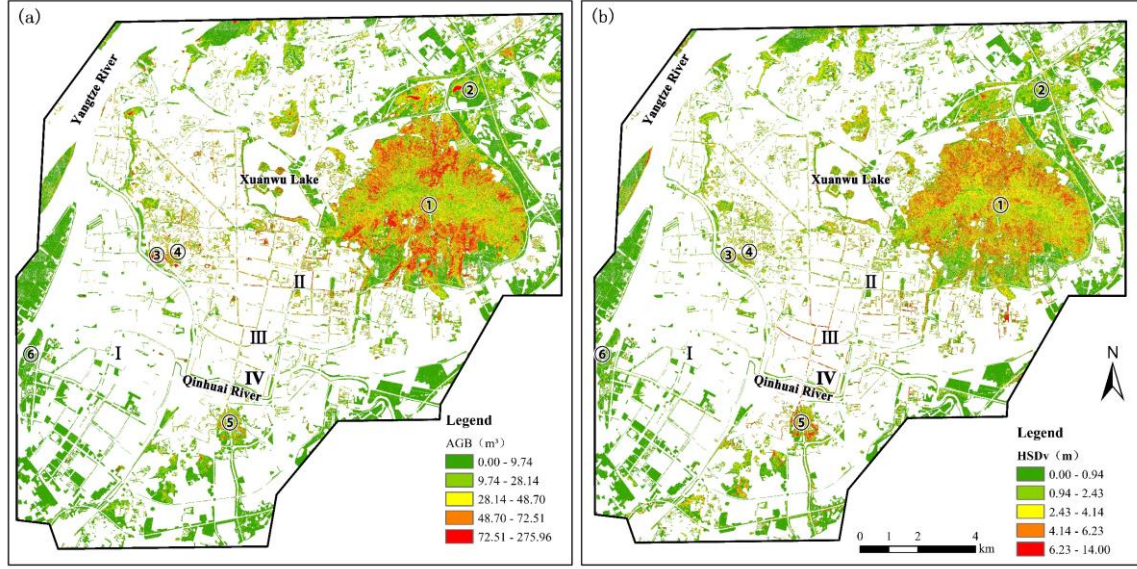


Fig 2 Aboveground biomass AGB and standard deviation of vegetation height HSD_V across Nanjing; a) Purple Mountain Park①, Jubao Mountain Park②, Shitoucheng Park ③, Qingliang Mountain Park④, Yuhuatai Scenic area⑤; b) Hexi new district(I), Xinjiekou-Laomendong(II- IV).

V_B gradually decreases from the city center to the periphery of the study area. V_B is highest in the central business district (CBD) of Nanjing between Xinjiekou (II) and Fuzimiao-Laomendong (Fig 3(a), III-IV). The CBD further exhibits a large variability in building heights (Fig. 3(b), II-IV). HSD_B is also elevated in commercial areas and in newly developed areas, such as the Hexi New Town area (Fig. 3(b), I), which is currently the subcenter of Nanjing.

The downtown area near the Qinhuai River, Xuanwu Lake, and Purple Mountain Park are dense areas with high nCR (Fig. 3(c)). These districts have experienced constant urban redevelopment and infill over time. Buildings with various uses and styles lead to complex

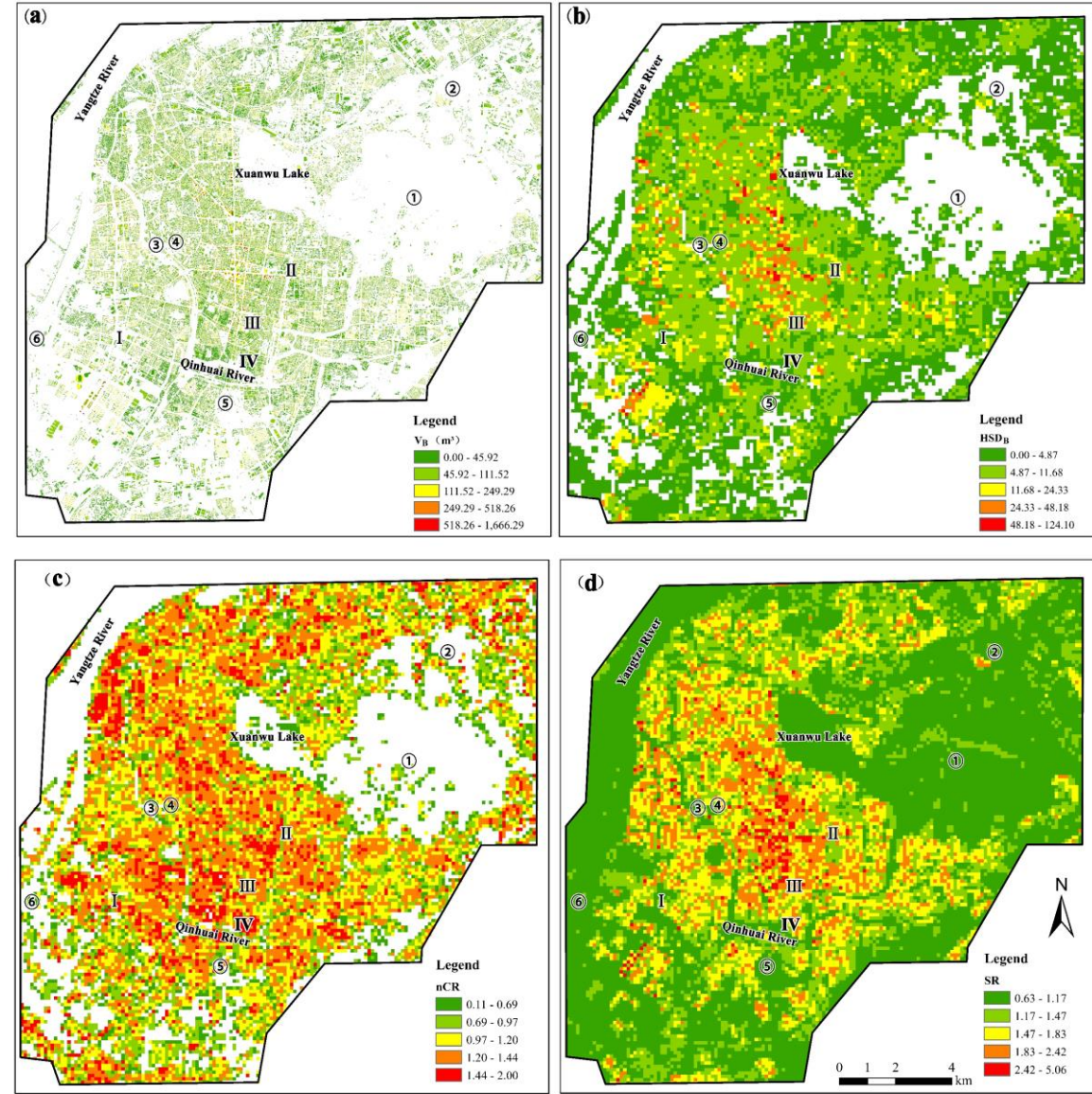


Fig 3 a) Distribution of building volume V_B , Xinjiekou (II) and Fuzimiao-Laomendong (III-IV); b) standard deviation of building height HSD_B , Hexi New District (I), Xinjiekou-Laomendong (II- IV); c) Building compactness ratio, nCR (c) and d) Surface roughness, SR .

3.1.2 Sky view factor (SVF)

The study area has an average SVF of 0.59. Open water bodies such as the Yangtze River and Xuanwu Lake have a SVF of 1, while forested areas such as Purple Mountain Park① and Jubao Mountain Park②, Yuhuatai Scenic Area ⑤, and the Nanjing Green Expo Park⑥ (Fig. 4) have a SVF of 0 or near 0 due to dense tree cover. The Old Town of Nanjing has dense buildings and a reduced SVF of generally less than 0.6, such as the Laomendong area (Fig. 4, IV). The SVF value of building roof varies with the height of the surrounding buildings in the area. In areas with similar building heights, the roof SVF is close to 1, while in areas with high HSD_B , the roof SVF is less than 1, e.g., in Xinjiekou (Fig. 4, II).

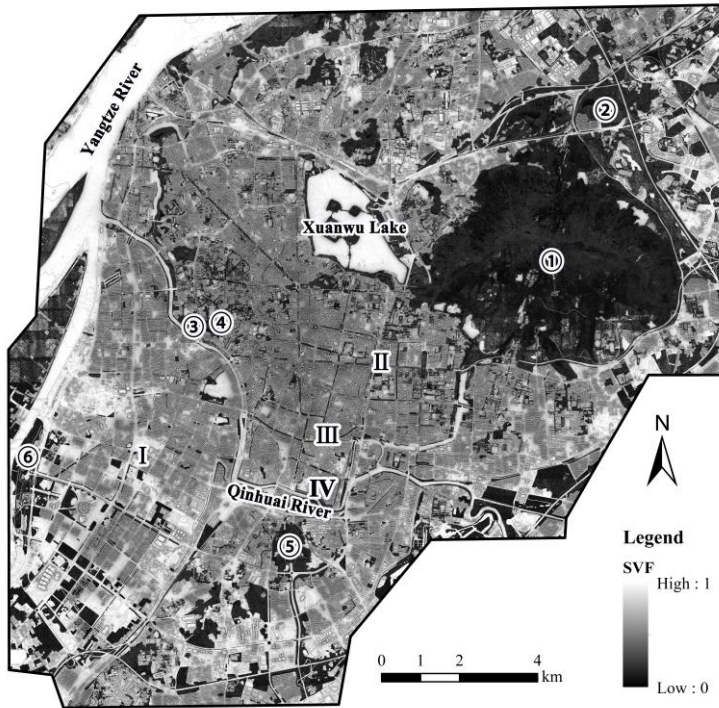


Fig. 4 Pattern of the SVF calculated using the UMEP model, Purple Mountain Park① and Jubao Mountain Park②, Yuhuatai Scenic Area⑤, and the Nanjing Green Expo Park⑥, Laomendong area (IV), Xinjiekou (II)

3.2 Spatiotemporal shadow patterns (SP)

Hourly shadow simulations for August 7, 2013 illustrate how shade travels throughout the day. Minimum shading occurs at noon when the solar elevation angle is largest. Tree-covered areas such as Purple Mountain Park are shaded throughout the day independent of the sun's position. In built-up areas, *SP* changes with solar elevation angle and building arrangement (Fig. 5). At 10:00h, shadows are to the west; at 12:00h, shadows are to the north; and at 14:00h and 16:00h, shadows are to the northeast and east, respectively. A comparison of *SP* maps at 10:00h and 14:00h reveals an asymmetrical shade pattern. Despite similar solar elevation angles, the heterogeneous urban form results in 30% shade coverage at 10:00h and 22% at 14:00h.

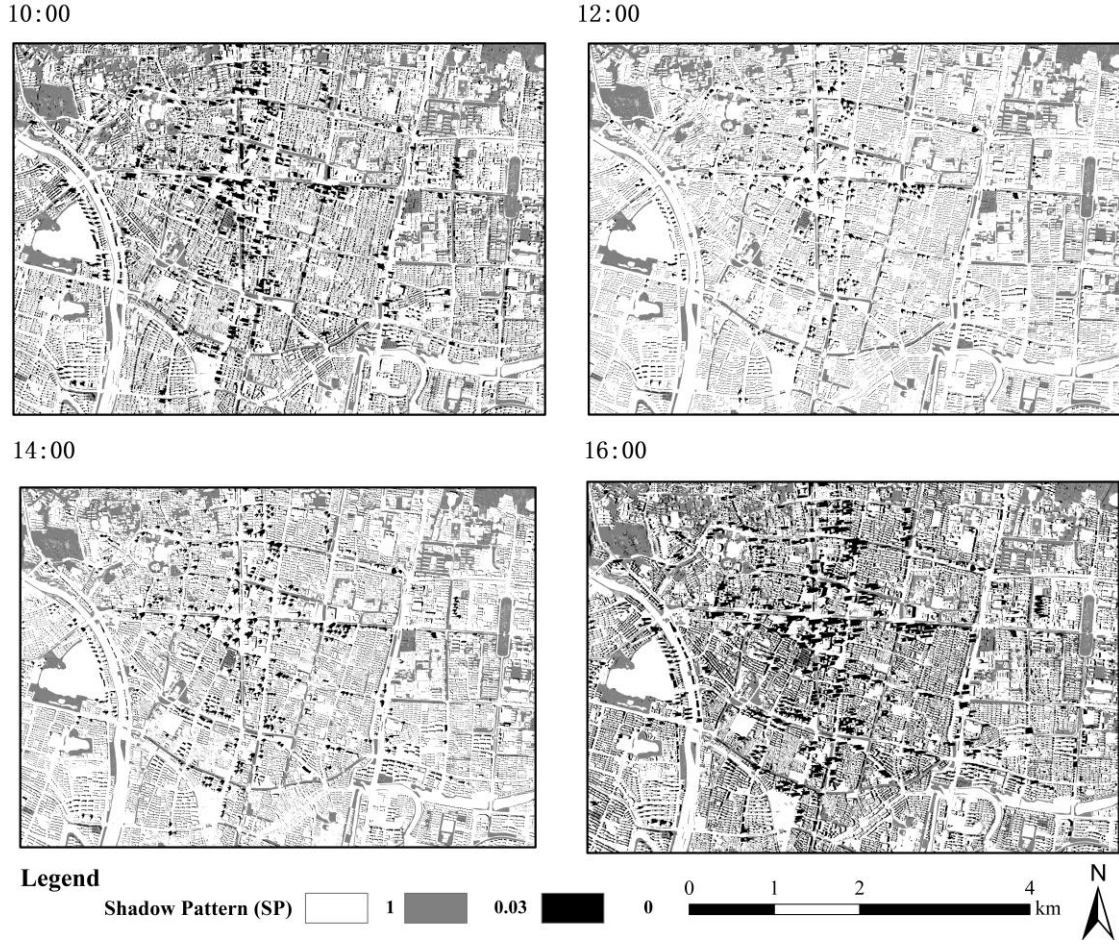


Fig. 5: Shadow pattern (*SP*) maps of the Xijiekou area (II) for select times of day: 10:00h, 12:00h, 14:00h, and 16:00h local time. Pixels denote shaded areas (0), sun-exposed areas (1), and areas shaded by vegetation (0.03).

3.3 Spatiotemporal T_{mrt} patterns and characteristics

Simulated T_{mrt} that is spatially averaged over the study area peaks at 61.4 ° at 14:00h and then decreases gradually (Fig. 6, Table 2). The highest T_{mrt} value across space and time is found at 12:00h (78.57 °). The standard deviation of T_{mrt} decreases as the day progresses, and stabilizes at around 2.3 ° after sunset, indicating that the thermal environment becomes more homogeneous across sites.

The Purple Mountain Park and surrounding areas maintain relatively stable thermal patterns with low T_{mrt} values in green spaces. During the day, built-up areas experience a T_{mrt} increase between 10:00h and 12:00h when shade is minimal. In contrast, impervious surfaces are mostly shaded by buildings in the afternoon, which reduces direct solar radiation and heat storage (e.g., in the Xijiekou area (II)). However, over extensive impervious surfaces with little vegetation such as parking lots and wide streets with low-rise buildings, T_{mrt} is elevated, e.g., in the Purple Mountain to the northeast and Hexi New Town to the southwest. Neighborhoods with forest cover exhibit lower T_{mrt} in the afternoon.

The minimum and maximum nocturnal T_{mrt} is 29.8 °C and 38.5 °C respectively (Table 2). The nocturnal average T_{mrt} varies slightly. The T_{mrt} is lower for areas with high SVF (open areas) than for densely built-up and vegetated areas. This is inverse to the thermal daytime pattern. At night, the longwave radiation emitted from the ground is trapped in densely built-up areas, which results in elevated T_{mrt} after sunset. At the same time, thermal patterns are more homogeneous and T_{mrt} differences are smaller across space due to the absence of incoming shortwave radiation.

Table 2 Differences in simulated T_{mrt} at different times of day.

Time	Mean (°C)	Max (°C)	Min(°C)	SD (°C)
10:00	56.53	72.97	37.73	12.05
12:00	60.90	78.57	39.97	12.06
14:00	61.39	77.68	41.62	11.79
16:00	55.53	69.09	41.32	9.45
20:00	33.28	38.49	30.70	2.29
22:00	32.39	37.59	29.82	2.28

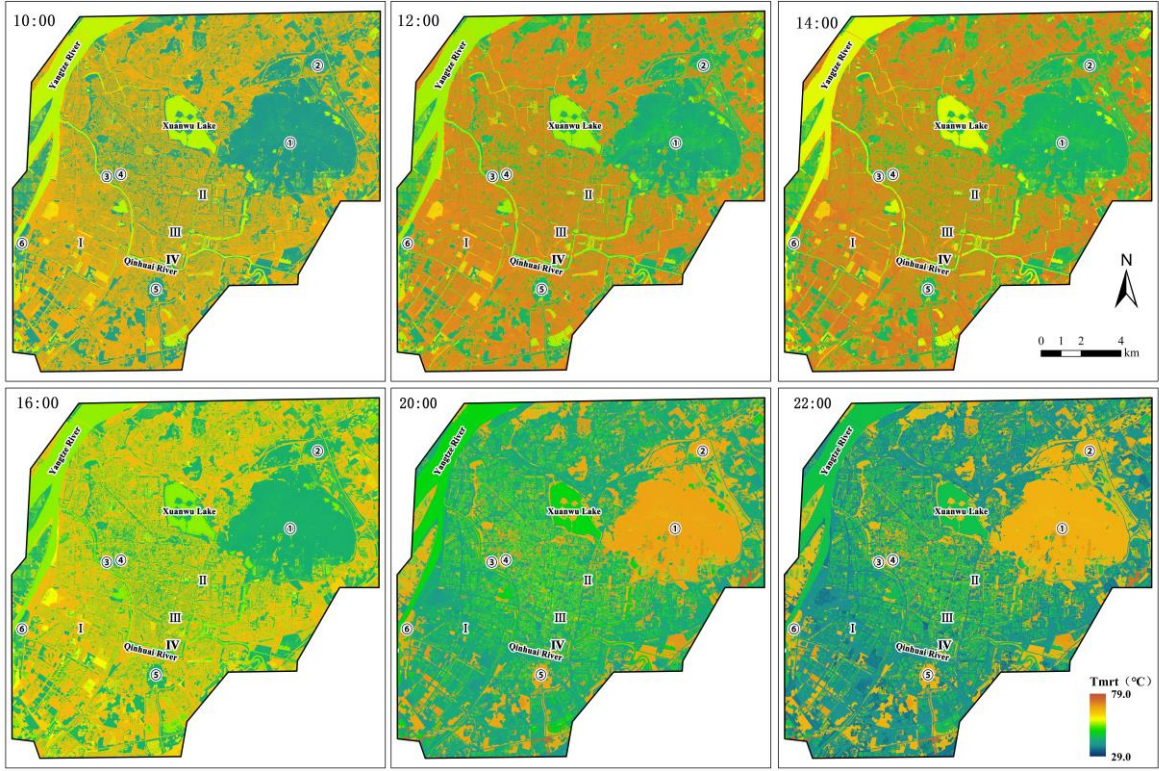


Fig. 6 T_{mrt} distribution (2-m resolution) in central Nanjing for August 7, 2013 at 10:00h, 12:00h, 14:00h, 16:00h, 20:00h and 22:00h.

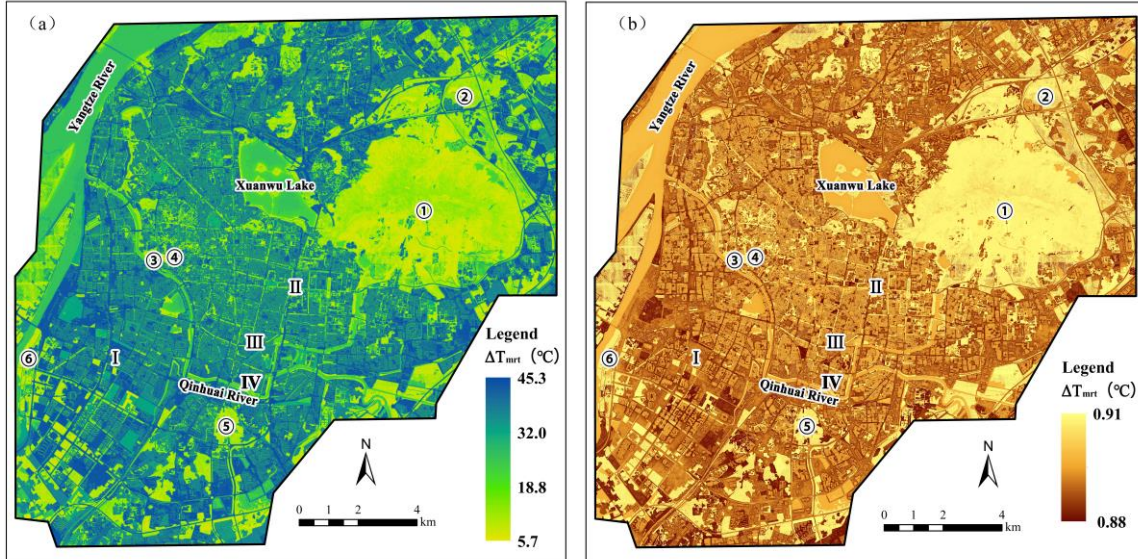


Fig. 7 Distribution of T_{mrt} differences (ΔT_{mrt}) (a) difference in 14:00h - 20:00h and (b) difference in 20:00h - 22:00h to indicate cooling rates.

Fig. 7 shows the distribution of T_{mrt} differences (a) difference in 14:00h - 20:00h and (b) difference in 20:00h - 22:00h to indicate cooling rates. ΔT_{mrt} is largest between 14:00h and 20:00h with a temperature difference of 45.3°C. Locations covered with water or vegetation showed a slightly lower change compared with built-up areas. The change in T_{mrt} after sunset is minimal (<1 °C), because T_{mrt} variability is mainly driven by solar radiation, which is absent at night. Radiative cooling rates after sunset are mainly driven by longwave radiation emitted from hot surfaces that retained heat.

3.4 Impact of 3-D urban landscape patterns on mean radiant temperature (T_{mrt})

A bivariate correlation analysis is performed to investigate the correlation between each metric and T_{mrt} (Table 3). After investigating multicollinearity, a stepwise multiple regression analysis is conducted to identify key factors that affect T_{mrt} (Table 4). Results from the bivariate correlation analysis show that all landscape indices have a significant relationship with T_{mrt} ($p < 0.01$) (Table 3). During the day, all vegetation metrics (AGB , HSD_v) are negatively correlated with T_{mrt} , while at night, the relationship is reversed. In contrast, all building metrics (V_B , HSD_B , nCR) and the vegetation and building-related integrated metrics (nCR , SR , SVF) show positive correlations with T_{mrt} , while at night, the reverse applies. The SP is positively correlated with T_{mrt} during the day; there is no SP at night.

The negative daytime correlation between vegetation metrics and T_{mrt} indicates cooling benefits of green infrastructure. The correlation is strongest at 12:00h and 14:00h when incoming solar radiation is near its peak and average T_{mrt} is largest (Table 2). The positive correlation of vegetation metrics and T_{mrt} at night combined with low SVF values in densely forested areas illustrates longwave radiation trapping as found by several authors (Oke, 1989; Colter et al., 2019; Middle et al., 2021)

The correlation between building-related landscape metrics (V_B , HSD_B , nCR) and T_{mrt} is strongest at peak T_{mrt} (at 12:00h and 14:00h). nCR is most significantly correlated with T_{mrt} . Among the vegetation and building-related integrated metrics, SP shows a very strong positive correlation with T_{mrt} during daytime; SR is positively and negatively correlated with T_{mrt} during the day and at night, respectively. SVF and SP have the highest correlation with T_{mrt} among all landscape metrics, because they characterize how much direct solar radiation an urban surface can receive.

Table 3 Bivariate correlations between 3D landscape indices and T_{mrt}

Data	T_{mrt_1000D}	T_{mrt_1200D}	T_{mrt_1400D}	T_{mrt_1600D}	T_{mrt_2000N}	T_{mrt_2200N}
AGB	-0.550**	-0.452**	-0.484**	-0.529**	0.579**	0.579**
HSD_v	-0.286**	-0.157**	-0.200**	-0.293**	0.307**	0.307**
V_B	0.199**	0.398**	0.334**	0.146**	-0.178**	-0.178**
HSD_B	0.184**	0.377**	0.313**	0.132**	-0.175**	-0.175**
nCR	0.349**	0.552**	0.489**	0.310**	-0.311**	-0.311**
SR	0.188**	0.412**	0.338**	0.125**	-0.155**	-0.155**
SVF	0.786**	0.577**	0.650**	0.766**	-0.851**	-0.851**
SP_{1000D}	0.875**	/	/	/	/	/
SP_{1200D}	/	0.693**	/	/	/	/
SP_{1400D}	/	/	0.744**	/	/	/
SP_{1600D}	/	/	/	0.818**	/	/

Note: Significance level: ** $p < 0.01$

SP is collinear with SVF with a variance inflation factor (VIF) greater than 10 (with $n > 10000$). At the same time, shade only existed during the day, so the SP variable is subsequently excluded from the multiple regression analysis. Table 4 summarizes the regression standardized coefficients between the 3-D urban landscape metrics and T_{mrt} showing a significant relationship ($P < 0.01$, except HSD_v at 10:00h).

SVF , building nCR , and AGB are three important time-invariant factors governing

outdoor T_{mrt} . SVF and building nCR have a significant warming effect on the local thermal environment in areas with high metric values that affect the radiation received and emitted by urban surfaces during the day.

SVF as a vegetation and building-related metric has the strongest positive daytime and negative nighttime impact on T_{mrt} . During the day, increasing building or vegetation height increases shade, therefore reducing heat storage of surfaces in the urban canyon. However, it also leads to more trapping of outgoing radiation at night. Open areas have a stronger ability to lose heat and lower T_{mrt} . Lastly, areas with little obstruction to air circulation also have lower T_{mrt} due to faster heat loss. The daytime vs. nighttime impacts of SVF require further investigation by considering the diurnal microclimate and solar altitude.

Higher nCR indicates compact buildings and larger building envelopes per volume. The building envelope, when its outer surface is heated by solar radiation to exceed the air temperature of the surrounding environment, will exchange heat with the environment through convection and longwave radiation, causing the surrounding temperature and T_{mrt} to rise (Givoni, 1998). After sunset, T_{mrt} decreases with increasing nCR , indicating that areas with complex building morphology cool faster than areas with low nCR values.

AGB is negatively correlated with T_{mrt} , during the day, revealing that urban green spaces play an important role in regulating the outdoor thermal environment. AGB affects T_{mrt} during the day by converting sensible heat into latent heat and by preventing the ground from absorbing solar radiation, resulting in lower temperatures in areas with high metric values, however, at night, higher AGB will contribute to heat trapping, which produces a mild warming effect and leads to a positive correlation with T_{mrt} .

Table 4 Results of the multi-variate linear stepwise regression between urban multi-dimensional landscape indices and T_{mrt} after eliminating collinear variables.

Model		Unstandardized Coefficients		Standardized Coefficients	t	Sig.
		B	Std. Error	Beta		
Dependent Variable:	(Constant)	38.140	0.171	--	223.599	0.000
T_{mrt_1000D}	AGB	-0.120	0.008	-0.095	-15.569	0.000
Adjusted R ² =0.809	HSD _v	0.074	0.032	0.013	2.320	0.020
	nCR	4.011	0.065	0.343	61.941	0.000
	SR	1.197	0.089	0.114	20.230	0.000
	SVF	22.087	0.154	0.788	143.045	0.000
Dependent Variable:	(Constant)	38.954	0.315	--	123.555	0.000
T_{mrt_1200D}	AGB	-0.157	0.011	-0.104	-14.773	0.000
Adjusted R ² =0.744	HSD _v	0.300	0.044	0.043	6.868	0.000
	V _B	0.025	0.006	0.046	4.030	0.000
	nCR	6.260	0.089	0.453	70.173	0.000
	SR	3.634	0.232	0.195	15.658	0.000
	SVF	20.404	0.213	0.614	95.763	0.000
Dependent Variable:	(Constant)	40.808	0.292	--	139.787	0.000
T_{mrt_1400D}	AGB	-0.140	0.010	-0.098	-14.269	0.000
Adjusted R ² =0.754	HSD _v	0.215	0.041	0.032	5.270	0.000
	V _B	0.023	0.006	0.044	3.940	0.000
	nCR	5.543	0.083	0.424	67.107	0.000
	SR	2.687	0.215	0.153	12.503	0.000
	SVF	21.213	0.197	0.676	107.523	0.000
Dependent Variable:	(Constant)	42.645	0.123	--	346.541	0.000
T_{mrt_1600D}	AGB	-0.096	0.007	-0.092	-14.613	0.000
Adjusted R ² =0.737	HSD _B	0.040	0.005	0.048	7.933	0.000
	nCR	3.343	0.057	0.349	58.928	0.000
	SVF	17.219	0.146	0.749	118.103	0.000
Dependent Variable:	(Constant)	36.874	0.037	--	990.239	0.000
T_{mrt_2000N}	AGB	0.025	0.001	0.096	20.870	0.000
Adjusted R ² =0.889	HSD _v	-0.028	0.005	-0.024	-5.716	0.000
	V _B	0.005	0.001	0.058	6.431	0.000
	HSD _B	-0.029	0.002	-0.140	-15.160	0.000
	nCR	-0.744	0.010	-0.316	-74.391	0.000
	SR	-0.111	0.029	-0.035	-3.869	0.000
	SVF	-4.797	0.024	-0.850	-201.526	0.000
Dependent Variable:	(Constant)	35.927	0.037	--	968.860	0.000
T_{mrt_2200N}	AGB	0.025	0.001	0.096	20.869	0.000
Adjusted R ² =0.889	HSD _v	-0.028	0.005	-0.024	-5.715	0.000
	V _B	0.005	0.001	0.058	6.430	0.000
	HSD _B	-0.029	0.002	-0.140	-15.160	0.000
	nCR	-0.742	0.010	-0.316	-74.389	0.000
	SR	-0.111	0.029	-0.035	-3.868	0.000
	SVF	-4.784	0.024	-0.850	-201.561	0.000

4. Discussion

4.1 Advancing urban thermal management and planning by coupling 3-D morphology with numerical model

Urban morphology created by buildings, vegetation, and other urban landscape elements influences the thermal environment (Oke, 1989). Areas with high AGB and HSD_V values are mostly located in parks and natural areas. In the city, 3-D vegetation patterns follow the age of urban developments, with higher AGB and HSD_V values in the Old Town of Nanjing and lower AGB and HSD_V values in new developments. High-density built-up areas are mainly located near the Qinhuai River-Xuanwu Lake-Purple Mountain with high V_B and HSD_B values. College Town and Old Town in the city center exhibit high building nCR ; the university and Old Town mostly have old, low-rise buildings, but new higher buildings have been added for infill development. The distribution of SR is consistent with that of densely built-up urban areas. The areas with low SVF (smaller than 0.6) are mainly distributed in the densely built-up Xinjiekou-Laomendong areas (Fig 1, Fig 4), where both the compact building arrangement and large building height reduce the SVF in street canyons. The SVF of highly vegetated areas is also relatively low. The SVF of building roofs is high in areas with low HSD_B . Shadow patterns are influenced by the solar elevation angle and building arrangement, and since most of the buildings in the study area face southwest and are arranged more compactly in the south-north direction than in the east-west direction, the shadow patterns in the southwest-northeast and southeast-northwest directions exhibit clear characteristics of temporal gradient changes (Fig. 5).

The spatial distribution of hourly T_{mrt} varies significantly in the central urban area of Nanjing. During the day, the southwestern part exhibits higher T_{mrt} than other areas, and T_{mrt}

of extensive impervious surfaces is elevated. In contrast, the Purple Mountain and surrounding areas covered with green spaces or water bodies maintain a relatively low T_{mrt} . However, after sunset, open areas in the center have a lower T_{mrt} and cooled faster than the densely built-up areas, vegetation-covered areas, and water bodies (Fig. 6, 7).

The statistical and correlation analyses of the 3-D urban landscape pattern metrics and T_{mrt} show that solar access of urban surfaces is an important factor affecting the daytime thermal environment (Table 3, 4). The SVF and building nCR are significantly positively correlated with T_{mrt} . Reducing solar access (increasing shade) during the day can effectively improve the urban thermal environment. At night, the cooling capacity of urban surfaces becomes the main factor that affects the urban thermal environment. The high correlation with nCR suggests that improving the thermal performance of the building envelope is one important way to increase thermal comfort outside and inside of buildings (Natephra et al., 2017). Considering the cooling effects of green building envelopes (vertical or roof greening) shown by previous studies (Perini et al., 2011; Zheng et al., 2021; Yin et al., 2017), greening the exterior of buildings (living building envelope) may have great potential as nature-based solutions to increase urban thermal comfort (Kim et al., 2016).

4.2 Current Limitations and Future Directions

The rapid development of LiDAR and other remote sensing techniques and advancements in computing power have facilitated the development of 3-D city models and derived 3-D landscape metrics to quantify the complex geometric structure of urban areas (Bonczak & Kontokosta, 2019). Linking these metrics with numerical model output yields more precise and accurate results on the urban thermal environment. Current models cannot directly calculate 3-D landscape metrics, which is a limitation that led to the use of SVF and

SP from UMEP, while other metrics had to be calculated from different data sources.

Since LiDAR data and meteorological forcing data used in this study are historical data, synchronously measured T_{mrt} data could not be obtained, resulting in an insufficient model validation. While real-world T_{mrt} values may deviate from simulations, the fundamental relationships discovered in the correlation and regression analyses are expected to remain valid. Previous studies have investigated the close relationship between urban building volume and population (Biljecki et al., 2016; et al., 2016; Maroko et al., 2019; Chen et al., 2021), which provided a novel approach to estimate population patterns for areas that do not have demographic information available. Based on this relationship, further assumptions can be made about the amount of anthropogenic heat due to increased population size and the number of people who are potentially experience increased heat load on their body outdoors due to elevated T_{mrt} .

The study illustrates how knowledge related to coupling 3-D urban morphology with numerical modeling can be used to moderate the undesirable consequences of urban development and help create more livable and resilient cities. T_{mrt} spatial patterns combined with population information will also be helpful to evaluate inequities of who is exposed to excessive heat and how heat impacts the quality of life and wellbeing. Finally, this approach has great potential to be used for building energy modeling and multi-scenario designs that consider building envelope greening to mitigate heat and improve outdoor and indoor thermal comfort.

5. Conclusions

This study investigated the impacts of 3-D urban landscape patterns on the outdoor thermal environment at an urban scale by coupling the 3-D urban landscape metrics

calculated from LiDAR point-clouds and the UMEP tool. Using LiDAR point-clouds, this study constructed an innovative building compactness measure (nCR) and implemented urban shadow pattern metrics and high-resolution SVF maps derived from UMEP output to facilitate a more realistic characterization of the 3-D urban landscape and promote an in-depth investigation of 3-D landscape patterns that affect the urban thermal environment.

By coupling the 3-D metrics with the UMEP integrated tool, T_{mrt} was simulated in the urban area using observed meteorological data as forcing. A bivariate correlation analysis showed that all 3-D urban landscape metrics are significantly correlated with T_{mrt} , indicating that 3D urban form plays an important and crucial role in shaping urban T_{mrt} . The results of a multi-variate linear stepwise regression analysis highlight that the 3-D urban morphology parameters AGB , nCR , and SVF are key variables governing the urban thermal environment. During the day, AGB is negatively correlated with T_{mrt} , while SVF and building nCR are positively correlated with T_{mrt} , an inverse relationship exists at night.

Our results provide a new perspective on managing urban form to help create thermally comfortable and livable environments based on fully considering the impact of 3-D urban landscape patterns, which can be quantified by the 3-D metrics derived from LiDAR. Results also highlight the offset effects and tradeoffs of these 3D metrics related to T_{mrt} , which requires further investigation in various localities to optimize urban form for improved outdoor thermal comfort.

Acknowledgments

This study was funded by the National Key R&D Program of China (No. 2017YFE0196000) and the National Natural Science Foundation of China (No. 51878328, 31670470).

References

- Abbasabadi, N., & Ashayeri, M. (2019). Urban energy use modeling methods and tools: A review and an outlook. *Building and Environment*, 161, 106270.
- Aboelata, A. (2020). Vegetation in different street orientations of aspect ratio (H/W 1: 1) to mitigate UHI and reduce buildings' energy in arid climate. *Building and Environment*, 172, 106712.
- Ali-Toudert, F., & Mayer, H. (2007). Thermal comfort in an east-west oriented street canyon in Freiburg (Germany) under hot summer conditions. *Theoretical and Applied Climatology*, 87(1-4), 223-237.
- Amiri, R., Weng, Q., Alimohammadi, A., & Alavipanah, S. K. (2009). Spatial-temporal dynamics of land surface temperature in relation to fractional vegetation cover and land use/cover in the Tabriz urban area, Iran. *Remote Sensing of Environment*, 113(12), 2606–2617.
- An, S. M., Kim, B. S., Lee, H. Y., Kim, C. H., Yi, C. Y., Eum, J. H., & Woo, J. H. (2014). Three-dimensional point cloud based sky view factor analysis in complex urban settings. *International Journal of Climatology*, 34(8), 2685–2701.
- Barlow, J. F. (2014). Progress in observing and modelling the urban boundary layer. *Urban Climate*, 10, 216-240.
- Biljecki, F., Arroyo Ohori, K., Ledoux, H., Peters, R., & Stoter, J. (2016). Population estimation using a 3D city model: A multi-scale country-wide study in the Netherlands. *PloS one*, 11(6), e0156808.
- Bonan, G. (2015). *Ecological climatology: concepts and applications*. Cambridge University Press.
- Bonczak, B., & Kontokosta, C. E. (2019). Large-scale parameterization of 3D building morphology in complex urban landscapes using aerial LiDAR and city administrative data. *Computers, Environment and Urban Systems*, 73, 126-142.

- Bowler, D. E., Buyung-Ali, L., Knight, T. M., & Pullin, A. S. (2010). Urban greening to cool towns and cities: A systematic review of the empirical evidence. *Landscape and Urban Planning*, 97(3), 147–155.
- Chen, H., Wu, B., Yu, B., Chen, Z., Wu, Q., Lian, T., ... & Wu, J. (2021). A New Method for Building-Level Population Estimation by Integrating LiDAR, Nighttime Light, and POI Data. *Journal of Remote Sensing*, 2021.
- Chen, L., Ng, E., An, X., Ren, C., Lee, M., Wang, U., & He, Z. (2012). Sky view factor analysis of street canyons and its implications for daytime intra- urban air temperature differentials in high- rise, high- density urban areas of Hong Kong: a GIS- based simulation approach. *International Journal of Climatology*, 32(1), 121–136.
- Chen, Y.-C., Lin, T.-P., & Matzarakis, A. (2014). Comparison of mean radiant temperature from field experiment and modelling: a case study in Freiburg, Germany. *Theoretical and Applied Climatology*, 118(3), 535–551.
- Chun, B., & Guldmann, J. M. (2014). Spatial statistical analysis and simulation of the urban heat island in high-density central cities. *Landscape and urban planning*, 125, 76-88.
- Chun, B., & Guldmann, J. M. (2018). Impact of greening on the urban heat island: Seasonal variations and mitigation strategies. *Computers, Environment and Urban Systems*, 71, 165-176.
- Colter, K. R., Middel, A. C., & Martin, C. A. (2019). Effects of natural and artificial shade on human thermal comfort in residential neighborhood parks of Phoenix, Arizona, USA. *Urban Forestry and Urban Greening*, 44.
- Darmanto, N. S., Varquez, A. C., & Kanda, M. (2017). Urban roughness parameters estimation from globally available datasets for mesoscale modeling in megacities. *Urban Climate*, 21, 243-261.
- Duan, G., & Takemi, T. (2021). Predicting urban surface roughness aerodynamic parameters using random forest. *Journal of Applied Meteorology and Climatology*, 999-1018.

- 1
- 2
- 3
- 4 540 Fernández, M. E., Picone, N., Gentili, J. O., & Campo, A. M. (2021). Analysis of the Urban
- 5
- 6 541 Energy Balance in Bahía Blanca (Argentina). *Urban Climate*, 37, 100856.
- 7
- 8
- 9 542 Gabey, A. M., Grimmond, C. S. B., & Capel-Timms, I. (2019). Anthropogenic heat flux:
- 10 543 advisable spatial resolutions when input data are scarce. *Theoretical and applied*
- 11
- 12 544 *climatology*, 135(1), 791-807.
- 13
- 14
- 15 545 Givoni, B. (1998). Climate Considerations in Building and Urban Design. John Wiley &
- 16 546 Sons
- 17
- 18
- 19 547 Grimmond, C. S. B., & Oke, T. R. (1999). Aerodynamic Properties of Urban Areas Derived
- 20 548 from Analysis of Surface Form. *Journal of Applied Meteorology*, 38(9), 1262–1292.
- 21
- 22
- 23
- 24 549 Grimmond, C. S. B., & Oke, T. R. (1999). Aerodynamic properties of urban areas derived
- 25 550 from analysis of surface form. *Journal of Applied Meteorology and Climatology*,
- 26 551 38(9), 1262-1292.
- 27
- 28
- 29
- 30 552 Hsieh, C. M., Li, J. J., Zhang, L., & Schwegler, B. (2018). Effects of tree shading and
- 31 553 transpiration on building cooling energy use. *Energy and Buildings*, 159, 382-397.
- 32
- 33
- 34
- 35 554 Hwang, R. L., Lin, T. P., & Matzarakis, A. (2011). Seasonal effects of urban street shading
- 36 555 on long-term outdoor thermal comfort. *Building and environment*, 46(4), 863-870.
- 37
- 38
- 39
- 40 556 Jenness, J. S. (2004). Calculating landscape surface area from digital elevation models.
- 41 557 *Wildlife Society Bulletin*, 32(3), 829-839.
- 42
- 43
- 44 558 Johnson, G. T., & Watson, I. D. (1984). The determination of view-factors in urban
- 45 559 canyons. *Journal of Climate and Applied Meteorology*, 23(2), 329–335.
- 46
- 47
- 48
- 49 560 Kidd, C., & Chapman, L. (2012). Derivation of sky-view factors from lidar data.
- 50 561 *International Journal of Remote Sensing*, 33(11), 3640–3652.
- 51
- 52
- 53 562 Kim, J., Hong, T., Jeong, J., Koo, C., & Jeong, K. (2016). An optimization model for
- 54 563 selecting the optimal green systems by considering the thermal comfort and energy
- 55 564 consumption. *Applied Energy*, 169, 682-695.
- 56
- 57
- 58
- 59
- 60
- 61
- 62
- 63
- 64
- 65

- Kong, F., Yan, W., Zheng, G., Yin, H., Cavan, G., Zhan, W., ... & Cheng, L. (2016). Retrieval of three-dimensional tree canopy and shade using terrestrial laser scanning (TLS) data to analyze the cooling effect of vegetation. *Agricultural and forest meteorology*, 217, 22-34.
- Kong, F., Yin, H., James, P., Hutyra, L. R., & He, H. S. (2014). Effects of spatial pattern of greenspace on urban cooling in a large metropolitan area of eastern China. *Landscape and Urban Planning*, 128, 35-47.
- Li, X., Li, W., Middel, A., Harlan, S. L., Brazel, A. J., & Turner, B. L. (2016). Remote sensing of the surface urban heat island and land architecture in Phoenix, Arizona: Combined effects of land composition and configuration and cadastral demographic economic factors. *Remote Sensing of Environment*, 174, 233-243.
- Li, Y., Schubert, S., Kropp, J. P., & Rybski, D. (2020). On the influence of density and morphology on the Urban Heat Island intensity. *Nature communications*, 11(1), 1-9.
- Lidar360 User Guide. GreenValley International Ltd, Berkeley, California. Available at the following (accessible on Oct. 2, 2021)
website:<https://greenvalleyintl.com/static/upload/file/20210817/1629190611196646.pdf>
- Lindberg, F., & Grimmond, C. S. B. (2011). Nature of vegetation and building morphology characteristics across a city: influence on shadow patterns and mean radiant temperatures in London. *Urban Ecosystems*, 14(4), 617-634.
- Lindberg, F., Grimmond, C. S. B., Gabey, A., Huang, B., Kent, C. W., Sun, T., ... & Zhang, Z. (2018). Urban Multi-scale Environmental Predictor (UMEP): An integrated tool for city-based climate services. *Environmental Modelling & Software*, 99, 70-87.
- Lindberg, F., Holmer, B., & Thorsson, S. (2008). SOLWEIG 1.0-Modelling spatial variations of 3D radiant fluxes and mean radiant temperature in complex urban settings. *International journal of biometeorology*, 52(7), 697-713.

- 591 Maragkogiannis, K., Kolokotsa, D., Maravelakis, E., & Konstantaras, A. (2014).
592 Combining terrestrial laser scanning and computational fluid dynamics for the study
593 of the urban thermal environment. *Sustainable Cities and Society*, 13, 207-216.
- 594 Maroko, A., Maantay, J., Pérez Machado, R. P., & Barrozo, L. V. (2019). Improving
595 population mapping and exposure assessment: three-dimensional dasymetric
596 disaggregation in New York City and São Paulo, Brazil. *Applied Geography*, 5(1-2),
597 45-57.
- 598 Michiles, A. A. dos S., & Gielow, R. (2008). Above-ground thermal energy storage rates,
599 trunk heat fluxes and surface energy balance in a central Amazonian rainforest.
600 *Agricultural and Forest Meteorology*, 148(6–7), 917–930.
- 601 Middel, A., & Krayenhoff, E. S. (2019). Micrometeorological determinants of pedestrian
602 thermal exposure during record-breaking heat in Tempe, Arizona: Introducing the
603 MaRTy observational platform. *Science of the Total Environment*, 687.
- 604 Middel, A., AlKhaled, S., Schneider, F. A., Hagen, B., & Coseo, P. (2021). 50 Grades of
605 Shade. *Bulletin of the American Meteorological Society*, 1–35.
- 606 Middel, A., Häb, K., Brazel, A. J., Martin, C. A., & Guhathakurta, S. (2014). Impact of
607 urban form and design on mid-afternoon microclimate in Phoenix Local Climate
608 Zones. *Landscape and Urban Planning*, 122, 16–28.
- 609 Middel, A., Lukasczyk, J., Maciejewski, R., Demuzere, M., & Roth, M. (2018). Sky View
610 Factor footprints for urban climate modeling. *Urban climate*, 25, 120-134.
- 611 Middel, A., Selover, N., Hagen, B., & Chhetri, N. (2016). Impact of shade on outdoor
612 thermal comfort—a seasonal field study in Tempe, Arizona. *International journal of
613 biometeorology*, 60(12), 1849-1861.
- 614 Motazedian, A., Coutts, A. M., & Tapper, N. J. (2020). The microclimatic interaction of a
615 small urban park in central Melbourne with its surrounding urban environment during
616 heat events. *Urban Forestry & Urban Greening*, 126688.

- Mirzaee, S., Özgun, O., Ruth, M., & Binita, K. C. (2018). Neighborhood-scale sky view factor variations with building density and height: A simulation approach and case study of Boston. *Urban climate*, 26, 95-108.
- Natephra, W., Motamedi, A., Yabuki, N., & Fukuda, T. (2017). Integrating 4D thermal information with BIM for building envelope thermal performance analysis and thermal comfort evaluation in naturally ventilated environments. *Building and Environment*, 124, 194-208.
- Nield, J. M., King, J., Wiggs, G. F., Leyland, J., Bryant, R. G., Chiverrell, R. C., ... & Washington, R. (2013). Estimating aerodynamic roughness over complex surface terrain. *Journal of Geophysical Research: Atmospheres*, 118(23), 12-948.
- Norton, B. A., Coutts, A. M., Livesley, S. J., Harris, R. J., Hunter, A. M., & Williams, N. S. G. (2015). Planning for cooler cities: A framework to prioritise green infrastructure to mitigate high temperatures in urban landscapes. *Landscape and Urban Planning*, 134, 127–138.
- Oke, T. R. (1981). Canyon geometry and the nocturnal urban heat island: comparison of scale model and field observations. *Journal of Climatology*, 1(3), 237–254.
- Oke, T. R. (1989). The micrometeorology of the urban forest. *Philosophical Transactions of the Royal Society of London. B, Biological Sciences*, 324(1223), 335-349.
- Oke, T. R. "Street design and urban canopy layer climate." *Energy and buildings* 11.1 (1988): 103-113.
- Park, Y., Guldmann, J. M., & Liu, D. (2021). Impacts of tree and building shades on the urban heat island: Combining remote sensing, 3D digital city and spatial regression approaches. *Computers, Environment and Urban Systems*, 88, 101655.
- Patz, J. A., Campbell-Lendrum, D., Holloway, T., & Foley, J. A. (2005). Impact of regional climate change on human health. *Nature* 2005 438:7066, 438(7066), 310–317.

- Peeters, A. (2016). A GIS-based method for modeling urban-climate parameters using automated recognition of shadows cast by buildings. *Computers, Environment and Urban Systems*, 59, 107-115.
- Peeters, A., Shashua-Bar, L., Meir, S., Shmulevich, R. R., Caspi, Y., Weyl, M., ... & Angel, N. (2020). A decision support tool for calculating effective shading in urban streets. *Urban Climate*, 34, 100672.
- Perini, K., & Magliocco, A. (2014). Effects of vegetation, urban density, building height, and atmospheric conditions on local temperatures and thermal comfort. *Urban Forestry & Urban Greening*, 13(3), 495-506.
- Perini, K., Ottelé, M., Fraaij, A. L. A., Haas, E. M., & Raiteri, R. (2011). Vertical greening systems and the effect on air flow and temperature on the building envelope. *Building and Environment*, 46(11), 2287-2294.
- Perkins, S. E., Alexander, L. V., & Nairn, J. R. (2012). Increasing frequency, intensity and duration of observed global heatwaves and warm spells. *Geophysical Research Letters*, 39(20), 20714.
- Petras, V., Newcomb, D. J., & Mitasova, H. (2017). Generalized 3D fragmentation index derived from lidar point clouds. *Open Geospatial Data, Software and Standards*, 2(1), 1-14.
- Rahman, M. A., Stratopoulos, L. M., Moser-Reischl, A., Zölch, T., Häberle, K. H., Rötzer, T., ... & Pauleit, S. (2020). Traits of trees for cooling urban heat islands: A meta-analysis. *Building and Environment*, 170, 106606.
- Ratti, C., & Richens, P. (1999). Urban texture analysis with image processing techniques. In *Computers in Building* (pp. 49-64). Springer, Boston, MA.
- Ratti, C., Di Sabatino, S., & Britter, R. (2006). Urban texture analysis with image processing techniques: winds and dispersion. *Theoretical and applied climatology*, 84(1), 77-90.

- Ronchi, S., Salata, S., & Arcidiacono, A. (2020). Which urban design parameters provide climate-proof cities? An application of the Urban Cooling InVEST Model in the city of Milan comparing historical planning morphologies. *Sustainable Cities and Society*, 63, 102459.
- Salata, F., Golasi, I., de Lieto Vollaro, A., & de Lieto Vollaro, R. (2015). How high albedo and traditional buildings' materials and vegetation affect the quality of urban microclimate. A case study. *Energy and Buildings*, 99, 32-49.
- Santamouris, M. (2014). On the energy impact of urban heat island and global warming on buildings. *Energy and Buildings*, 82, 100–113.
- Sato, Y., Higuchi, A., Takami, A., Murakami, A., Masutomi, Y., Tsuchiya, K., ... & Nakajima, T. (2016). Regional variability in the impacts of future land use on summertime temperatures in Kanto region, the Japanese megacity. *Urban Forestry & Urban Greening*, 20, 43-55.
- Shareef, S., & Abu-Hijleh, B. (2020). The effect of building height diversity on outdoor microclimate conditions in hot climate. A case study of Dubai-UAE. *Urban Climate*, 32, 100611.
- Sharmin, T., Kabir, S., & Rahaman, M. (2012). A study of thermal comfort in outdoor urban spaces in respect to increasing building height in Dhaka. *AIUB Journal of Science and Engineering*, 11(1).
- Solcerova, A., van de Ven, F., Wang, M., Rijdsdijk, M., & van de Giesen, N. (2017). Do green roofs cool the air? *Building and Environment*, 111, 249–255.
- Thorsson, S., Lindberg, F., Eliasson, I., & Holmer, B. (2007). Different methods for estimating the mean radiant temperature in an outdoor urban setting. *International Journal of Climatology: A Journal of the Royal Meteorological Society*, 27(14), 1983-1993.

- 693 Tomás, L., Fonseca, L., Almeida, C., Leonardi, F., & Pereira, M. (2016). Urban population
694 estimation based on residential buildings volume using IKONOS-2 images and lidar
695 data. *International Journal of Remote Sensing*, 37(sup1), 1-28.
- 696 Unger, J. (2009). Connection between urban heat island and sky view factor approximated
697 by a software tool on a 3D urban database. *International Journal of Environment and
698 Pollution*, 36(1-3), 59-80.
- 699 Wong, N. H., & Yu, C. (2005). Study of green areas and urban heat island in a tropical city.
700 *Habitat International*, 29(3), 547-558.
- 701 Wonorahardjo, S., Sutjahja, I. M., Mardiyati, Y., Andoni, H., Thomas, D., Achsani, R. A.,
702 & Steven, S. (2020). Characterising thermal behaviour of buildings and its effect on
703 urban heat island in tropical areas. *International Journal of Energy and Environmental
704 Engineering*, 11(1), 129-142.
- 705 Xu, X.Z., Zheng, Y.F., Yin, J.F., Wu, R.J., 2011. Characteristics of high temperature and
706 heat wave in Nanjing City and their impacts on human health. *Chin. J. Ecol.*30 (12),
707 2815-2820 (in Chinese).
- 708 Yang, X., & Li, Y. (2015). The impact of building density and building height
709 heterogeneity on average urban albedo and street surface temperature. *Building and
710 Environment*, 90, 146-156.
- 711 Yin, H., Kong, F., Middel, A., Dronova, I., Xu, H., & James, P. (2017). Cooling effect of
712 direct green façades during hot summer days: An observational study in Nanjing,
713 China using TIR and 3DPC data. *Building and Environment*, 116, 195-206.
- 714 Zakšek, Klemen, Oštir, Kristof, & Kokalj, Žiga. (2011). Sky-view factor as a relief
715 visualization technique. *Remote Sensing*, 3(2), 398-415.
- 716 Zellweger, F., De Frenne, P., Lenoir, J., Rocchini, D., & Coomes, D. (2019). Advances in
717 microclimate ecology arising from remote sensing. *Trends in Ecology & Evolution*,
718 34(4), 327-341.

- 719 Zhang, Y., Middel, A., & Turner, B. L. (2019). Evaluating the effect of 3D urban form on
720 neighborhood land surface temperature using Google Street View and
721 geographically weighted regression. *Landscape Ecology*, 34(3), 681–697.
- 722 Zhang, Y., Sun, C., Bao, Y., & Zhou, Q. (2018). How surface roughness reduces heat
723 transport for small roughness heights in turbulent Rayleigh–Bénard convection.
724 *Journal of Fluid Mechanics*, 836, R2.
- 725 Zhang, Y., Zhang, L. N., Yang, C. D., Bao, W. D., & Yuan, X. X. (2011). Surface area
726 processing in GIS for different mountain regions. *Forestry Studies in China*, 13(4),
727 311-314.
- 728 Zheng, X., Kong, F., Yin, H., Middel, A., Liu, H., Wang, D., ... & Lensky, I. (2021).
729 Outdoor thermal performance of green roofs across multiple time scales: A case study
730 in subtropical China. *Sustainable Cities and Society*, 70, 102909.
- 731 Zhu, R., Wong, M. S., You, L., Santi, P., Nichol, J., Ho, H. C., ... & Ratti, C. (2020). The
732 effect of urban morphology on the solar capacity of three-dimensional cities.
733 *Renewable Energy*, 153, 1111-1126.
- 734 Zimble, D. A., Evans, D. L., Carlson, G. C., Parker, R. C., Grado, S. C., & Gerard, P. D.
735 (2003). Characterizing vertical forest structure using small-footprint airborne LiDAR.
736 *Remote sensing of Environment*, 87(2-3), 171-182.
- 737